

Microphysical variability in southeast Pacific Stratocumulus clouds: Synoptic conditions and radiative response

D. Painemal¹ and P. Zuidema¹

[1]{Rosenstiel School of Marine and Atmospheric Sciences University of Miami}

Correspondence to: D. Painemal (dpainemal@rsmas.miami.edu)

Abstract

Synoptic and satellite-derived cloud property variations for the southeast Pacific stratocumulus region associated with changes in coastal satellite-derived cloud droplet number concentrations (N_d) are explored. MAX and MIN N_d composites are defined by the top and bottom terciles of daily area-mean N_d values over the Arica Bight, the region with the largest mean oceanic N_d , for the five October months of 2001, 2005, 2006, 2007 and 2008. The ability of the satellite retrievals to capture composite differences is assessed with ship-based data. N_d and ship-based accumulation mode aerosol concentrations (N_a) correlate well ($r=0.65$), with a best-fit aerosol activation value $\frac{d \ln N_d}{d \ln N_a}$ of 0.56 for pixels with $N_d > 50 \text{ cm}^{-3}$. The adiabatically-derived MODIS cloud depths also correlate well with the ship-based cloud depths ($r=0.7$), though are consistently higher (mean bias of almost 60 m). The MAX- N_d composite is characterized by a weaker subtropical anticyclone and weaker winds both at the surface and the lower free troposphere than the MIN- N_d composite. The MAX- N_d composite clouds over the Arica Bight are thinner than the MIN- N_d composite clouds, have lower cloud tops, lower near-coastal cloud albedos, and occur below warmer and drier free tropospheres (as deduced from radiosondes and NCEP Reanalysis). CloudSat radar reflectivities indicate little near-coastal precipitation. The co-occurrence of more boundary-layer aerosol/higher N_d within a more stable atmosphere suggests a boundary layer source for the aerosol, rather than the free troposphere.

The MAX- N_d composite cloud thinning extends offshore to 80°W, with lower cloud top heights out to 95°W. At 85°W, the top-of-atmosphere shortwave fluxes are significantly higher (~50%) for the MAX- N_d composite, with thicker, lower clouds and higher cloud fractions than for the MIN- N_d composite. The change in N_d at this location is small (though positive), suggesting that the MAX-MIN N_d composite differences in radiative properties primarily reflects synoptic changes. Circulation anomalies and a one-point spatial correlation map reveal a weakening of the 850 hPa southerly winds decreases the free tropospheric cold temperature advection. The resulting increase in the static stability along 85°W is highly correlated to the increased cloud fraction, despite accompanying weaker free tropospheric subsidence.

1. Introduction

The subtropical cloud-capped marine boundary layer has a strong climate impact through the decks' high solar reflectivity whereas the emitted long-wave radiation remains close to that of surface emission under clear skies (Hartmann et al., 1992). A deeper understanding of the processes affecting the radiative properties of maritime warm clouds, both large-scale and microphysical, is necessary for developing confidence in future climate predictions. This is becoming particularly important as more aerosol indirect effects become incorporated into climate models. Currently only the cloud albedo

effect $\left(\frac{\partial A}{\partial N_d}\right)_{lwp,met}$, or the change in cloud albedo A with cloud droplet number N_d , all else

held constant, Twomey, 1977), is considered in the Intergovernmental Panel on Climate Change (IPCC) 2007 assessment. Other effects, such as influences on the cloud albedo

through changes in liquid water path (LWP) induced by changes in N_d $\left(\frac{\partial A}{\partial(lwp)} \frac{\partial(lwp)}{\partial N_d}\right)_{met}$,

this includes the cloud lifetime effect (Albrecht, 1989)), are not yet formally included in the IPCC assessment. This acknowledges gaps in our understanding that could bring the latest IPCC estimates of -1.3 W m^{-2} [-0.5 to -2.2 W m^{-2} confidence range] for the aerosol direct forcing plus cloud albedo effect closer in line to a more moderate observational range for all aerosol direct and indirect effects of -1.1 W m^{-2} [-0.7 to -1.5 W m^{-2} confidence range] (Randall et al., 2007; Murphy et al., 2009).

Satellite-derived examples of cloud-aerosol radiative compensations include Han et al. (2002) and Matsui et al. (2006); both show more aerosols are often associated with lower liquid water paths. A tenet of the cloud lifetime effect, that higher LWPs are associated with longer cloud lifetimes (through precipitation suppression), has also recently been called into question (Christensen et al., 2009). Theoretical and modeling support for these observations has come from, among others, Jiang et al. (2002) and Ackerman et al. (2004), with more discussion in Stevens and Feingold (2009).

Dynamic compensation of aerosol indirect effects draws attention to the need to control for meteorological forcings, a difficulty in both modeling and observational assessments. Atmospheric static stability is often chosen as a meteorological control variable (e.g., Matsui et al., 2006), because static stability correlates well with stratocumulus cloud fraction at seasonal scales (Klein and Hartmann, 1993). Matsui et al. (2006) observed that cloud droplet sizes tend to be the smallest under strong inversions as well as within polluted environments. Mauger and Norris (2007) further examined the static stability of parcel back-trajectories of satellite-derived aerosol and cloud properties, and found that the covariation of aerosol amount and cloud fraction with static stability could increase with meteorological history.

The southeast Pacific stratocumulus deck is one region where aerosol impacts on cloud microphysics are potentially significant, with Bennartz (2007) and Wood et al. (2008) showing large ($> 200 \text{ cm}^{-3}$) cloud droplet number concentrations retrieved from MODerate resolution Imaging Spectroradiometer (MODIS) data along the Peru and Chile coast (17°S - 32°S), also shown here in Fig. 1. Though less clear from satellite imagery, measurements taken during the VAMOS Ocean-Coupled-Atmosphere-Land-Study Regional Experiment (VOCALS-REx; Wood and Mechoso, 2008) provide evidence of anthropogenic emissions as far west as 85°W (Hawkins et al., 2010). Bennartz (2007) speculated that the downwind transport of polluted air affected the microphysics of these clouds. This is plausible for the southeast Pacific where the Andes dictate along-shore winds that can transport aerosol from the more developed southern regions (the capital city of Chile, Santiago, is located near 33°S) to the north. Huneus et al. (2006) hypothesized instead that entrainment of polluted free-tropospheric air north of 25°S could be responsible for the N_d increases. At more northern latitudes the Andes protect the

deck from boundary-layer aerosol-laden continental outflow, but high-altitude copper smelters emit sulfate aerosols above the marine boundary layer.

Holistic regional assessments relying on satellite data, available local data, and reanalyses help provide background understanding for further regional aerosol-cloud interaction assessments. In this study, we focus further on understanding the meteorology and cloud macrophysical variability associated with N_d variability in the southeast Pacific stratocumulus region. An underlying premise is that the differences in cloud properties associated with the largest differences in N_d are likely to reflect synoptic influences, rather than the effect of cloud-aerosol interactions.

The large-scale circulation is depicted using the NCEP/NCAR Reanalysis. The Reanalysis is capable of resolving the main circulation features away from the coastline (Garreaud et al., 2001) and has been used successfully as a boundary forcing for more detailed regional simulations (e.g., Garreaud et al., 2004). The reanalysis is also known to underestimate the boundary layer depth, cloud fraction, and cloud liquid water path (e.g., Bretherton et al., 2004). Instead, cloud properties (cloud top height, fraction, liquid water path/thickness and droplet number) are derived primarily from MODIS data. The retrievals are aided by frequently overcast skies, relatively homogenous cloud conditions, and favorable sun-satellite viewing geometries (e.g., Kato and Marshak, 2009). Satellite-derived cloud droplet numbers (e.g., Bennartz, 2007) serve as an aerosol proxy, avoiding issues with satellite retrievals of clear-sky aerosol properties (e.g., Loeb and Schuster, 2008).

Further averaging of daily satellite data into composites also reduces the influence of random error. The analysis approach here is based on satellite and NCEP Reanalysis composites, with the composites defined through the upper and lower terciles of the satellite-retrieved cloud droplet numbers above the Arica Bight. A composite analysis approach also allows us to keep issues with the NCEP Reanalysis representation near the coastline and Andes mountains in perspective: these issues are demonstrated in comparisons to coastal radiosonde profiles of temperature, moisture and wind, and discourage coastal Lagrangian backtrajectory calculations. The composite analysis was applied to five October months of daily data. This month corresponds to the regional climatological maximum of the stratocumulus (Sc) deck (Klein and Hartmann, 1993),

and the focus on October months alone is intended to minimize influences from the seasonal progression. Our approach complements more thorough single case studies such as Huneus et al. (2006) and provides a context for VOCALS-REx analyses. We selected four October months coincident with NOAA research cruises (2001, 2005, 2006 and 2007), while October 2008 coincides with the VOCALS Regional Experiment. This was done so that the satellite retrievals could be compared to the ship-based measurements. The dataset and methodology are detailed in Section 2, composite results are described in Section 3, the regional circulation is discussed in Section 4, precipitation characteristics in Section 5, and concluding remarks in Section 6. The ship-satellite comparisons are included in Appendix.

2. Data and Methods

The composite analysis relies on daytime Terra level 3 data at $1^\circ \times 1^\circ$ spatial resolution; at this latitude, the daily-mean values for each platform are effectively regridded individual swath data. The daytime Terra overpass was previously found to be the MODIS overpass most representative of daily-mean conditions (Zuidema et al., 2009). MODIS cloud top temperatures, derived from separate day and nighttime $11 \mu\text{m}$ equivalent brightness temperatures, were used to estimate a satellite cloud top height, and rely on a depth-varying lapse rate, proportional to the inverse of the cloud top height, inferred from the open-ocean cruise radiosondes (see Zuidema et al., 2009, for full detail). These are shown to capture daily synoptic-scale variations reasonably well within Painemal et al. (2010) and agree well with airborne radar observations of cloud top made during VOCALS-REx (Rahn and Garreaud, 2010).

Estimates of the all-sky shortwave fluxes (SW) at the top of the atmosphere were obtained from the Clouds and Earth's Radiant Energy System (CERES, Wielicki et al. 1996) instrument on board the Terra platform. The CERES data allow for a net radiative assessment that is somewhat independent of the plane-parallel radiative transfer approximation. We used the radiometric measurements from the shortwave channel ($0.3 - 5 \mu\text{m}$), and spatially averaged Single Scanner Footprint data to a $1^\circ \times 1^\circ$ spatial resolution. These data were only available for October 2001, 2005, and 2006. The occurrence of

precipitation was determined from CloudSat radar reflectivity data (the Cloud-Geometrical-Profile product; Stephens et al., 2002) from October 2006, 2007 and 2008. Surface winds were provided by the satellite scatterometer QuikSCAT at a $0.25^\circ \times 0.25^\circ$ resolution; we only used the evening pass (1800 LT) data. Non-satellite data sources are the NCEP/NCAR reanalysis (Kalnay et al. 1997) meteorological fields, with a horizontal resolution of $2.5^\circ \times 2.5^\circ$, and daily radiosonde observations at Antofagasta (23.43°S , 70.43°W , 120 a.m.s.l.) available only at 1200 UTC (0800 LT) and interpolated to a consistent 50 hPa vertical resolution.

We combined MODIS Collection 5 cloud effective radius (r_e) and cloud optical thickness (τ) retrievals (Platnick et al., 2003) to produce values for N_d and cloud depth (H_{sat}), and used a temperature threshold of 273 K to select for warm, liquid-only clouds. MODIS retrievals of cloud optical depth and effective radius are routinely available, but small droplet sizes do not unambiguously indicate aerosol loading (e.g., Schuller et al., 2003). Instead, we estimated N_d and cloud depth (H_{sat}) from a combination of r_e (2.1 micron channel) and τ assuming adiabatic conditions (e.g. Bennartz, 2007, Szczodrak et al. 2001). This allows for a separation of macrophysical and microphysical cloud property measures, and in addition facilitates a comparison to the ship-based measurements of accumulation-mode aerosol N_a and cloud depth H_{ship} , shown in the Appendix.

H_{sat} is estimated from the adiabatically-derived liquid water path (LWP) using

$$LWP = \frac{\Gamma_{ad} H_{sat}^2}{2} \text{ as}$$

$$H_{sat} = \sqrt{\frac{2}{\Gamma_{ad}} \frac{5}{9} \rho_w \cdot r_e \cdot \tau} \quad (1)$$

where ρ_w is the density of water and Γ_{ad} is the adiabatic lapse rate of liquid water content with height. Previous assessments show good agreement between adiabatically-derived MODIS LWPs and satellite microwave-derived LWPs for overcast marine stratocumulus (e.g., Borg and Bennartz 2007; Seethala and Horvath, 2010). Sounding-derived Γ_{ad} values reveal that the lower, warmer coastal clouds have typical values between $2.1\text{-}2.3 \times 10^{-3} \text{ g m}^{-4}$, while clouds west of 75°W have values between $1.8\text{-}2.0 \times 10^{-3} \text{ g m}^{-4}$. Near-coastal liquid water content profiles in VOCALS-REx aircraft data often show

diminished values near cloud top because of cloud top entrainment, which reduces the effective Γ_{ad} , while profiles from further offshore are close to adiabatic (also seen in Zuidema et al., 2005). With this in mind, we rely on a constant Γ_{ad} value of $2.0 \times 10^{-3} \text{ g m}^{-4}$, and approximate its uncertainty at 10%.

The satellite estimate of cloud droplet concentration is based on

$$N_d = \Gamma_{ad}^{1/2} \frac{10^{1/2}}{4\pi\rho_w^{1/2}k} \cdot \frac{\tau^{1/2}}{r_e^{5/2}} \quad (2)$$

following Szczodrak et al. (2001). The parameter k corresponds to the cube of the ratio between the volume mean radius and the effective radius and is assumed constant at 0.8 (Martin et al., 1994).

Details of an error analysis for the satellite-derived estimates of N_d and H_{sat} are shown in the Appendix, and include comparisons to ship-based measurements of accumulation-mode aerosol concentration N_a and of cloud depth H_{ship} . Robust conclusions include good correlations between both cloud depth estimates and between N_a and N_d . We find a slightly higher value for $\frac{d \ln N_d}{d \ln N_a}$ than previously reported for Pt. Reyes, California (0.56 vs 0.48; McComiskey et al., 2009; Quaas et al., 2009). H_{sat} values often exceed H_{ship} (mean offset of 57 m) seemingly indicating superadiabatic satellite-derived LWPs. An explanation is currently lacking though ongoing work suggests a systematic MODIS effective radius overestimate may be one possibility. Further cloud depth values shown here do not correct for this bias.

3. Observational Composites

The satellite-ship comparisons of cloud depth and cloud droplet number shown in the Appendix, and for satellite-derived cloud top heights within Zuidema et al. (2009), provide confidence in the ability of the MODIS retrievals to represent the stratocumulus macro- and microphysics. Our composite analysis is based on the N_d variability over the apparently most-polluted region, the Arica Bight, defined here to span 71.5°W - 75.5°W and 18.5°S - 25.5°S (box in Fig. 1). Only scenes with at least 70% of their satellite pixels classified as overcast were used; this selection bias is discussed in Section 6. Such

overcast days occurred on 77% (120 days) of the total days. As seen in Fig. 1, mean LWP values are small ($< 70 \text{ g m}^{-2}$) over the region with the largest N_d .

Days are composited by the daily spatial-mean $\overline{N_d}$ over the Arica Bight into the highest and lowest terciles (40 and 42 overcast days each), labeled hereafter as MAX ($\overline{N_d} > 215.8 \text{ cm}^{-3}$) and MIN ($\overline{N_d} < 161.6 \text{ cm}^{-3}$) respectively. MAX-MIN N_d composite differences (Fig. 2, colors) are a maximum by construction between 18°S - 27°S with values higher than 120 cm^{-3} , and a westward extension of about 8° . Near Antofagasta (23.43°S ; small black square) the N_d changes reach their maximum value of 160 cm^{-3} , while the maximum climatological-mean N_d values occur further north near 20°S . Even further north along the Peruvian coast (north of 15°S), the cloud droplet number concentrations are slightly higher within the MIN- N_d composite than the MAX- N_d composite (negative values in Fig. 2). MAX-MIN N_d composite differences in LWP reveal decreased LWPs east of 85°W ($\sim 20 \text{ g m}^{-2}$) during the MAX- N_d composite, along with increased LWPs ($10\text{-}30 \text{ g m}^{-2}$) west of 85°W (Fig. 2), in one early indication of a dynamical compensation to the cloud albedo for near-coastal microphysical changes.

Time series of mean surface wind speeds (20°S - 30°S , 70°W - 90°W), mean cloud top heights alongshore (20°S - 30°S , 70°W - 80°W), and mean offshore 500 hPa geopotential heights (15°S - 35°S , 70°W - 100°W , approximately the location of the climatological anticyclone) are shown along with the occurrence of MAX (dark triangles) and MIN (open circles) N_d days in Fig. 3. These locations were chosen to exemplify synoptic differences between MAX and MIN cases: MAX (MIN) N_d days are more likely co-occur with weaker (stronger) coastal winds (Fig. 3a) and shallower coastal boundary layers (Fig. 3b), also shown in Fig. 4, and enhanced offshore mid-tropospheric geopotential heights (Fig. 3c). About one-half/two-thirds of the MIN/MAX N_d days, respectively, occur in groups of three or more days. Some interannual variability is evident as well, with more MIN N_d cases occurring during 2007, coinciding with a weak cool ENSO phase, and more MAX N_d cases than MIN N_d cases occurring during 2001 and 2008, when more intense observational campaigns, the Eastern Pacific Investigation of Climate (Bretherton et al., 2004) and VOCALS-REx, visited the region.

3.1 Satellite-derived composite characteristics

The mean and MAX-MIN N_d difference regional circulation patterns are shown in Fig. 5 panels a and b respectively. The anticyclone is strengthened offshore (85°W-95°W) during the MIN N_d composite, with stronger surface winds and a strengthened coastal jet near 33°S. Surface winds are light within both composites at the northern end of the Arica Bight, where changes in N_d are also modest. Mean October values along with MAX-MIN N_d composite difference values are shown for the MODIS-derived cloud top height (Fig. 5c), cloud depth (Fig. 5d), cloud fraction (Fig. 5e), and top-of-atmosphere CERES shortwave fluxes (Fig. 5f). Boundary layer depths are shallower for the MAX N_d composite by 200 m to 350 m over a broad domain extending beyond the Arica Bight (Fig. 5c). Over the Arica Bight and along 80°W, these changes are associated with thinner clouds for the MAX N_d composite (Fig. 5d), by up to 50 m. West of 80°W, the pattern reverses, and clouds are slightly thicker for the MAX N_d composite than for the MIN N_d composite.

The mean MODIS cloud fraction is a maximum parallel to the Peruvian coast (contours, Fig. 5e), with the mean values in the top-of-atmosphere shortwave fluxes following a similar spatial pattern (Fig. 5f). Cloud fractions are diminished by about 5% over the Arica Bight for the MAX composite relative to the MIN composite, remain approximately the same off the coast of Peru, and increase significantly elsewhere – by up to 20% near 85°W, 25°S. The variations in the top-of-atmosphere shortwave fluxes (Fig. 5f) are broadly consistent with the cloud fraction changes. Over the Arica Bight, the MAX-MIN composite change in top-of-atmosphere SW fluxes is negative near the coast, and increases 500 km offshore. This reflects the compensation between increased brightening from a higher N_d , and decreased brightening from a thinner cloud. Near the coast the cloud thinning ends up dominating radiatively, while further offshore the small increase in N_d more than offsets reductions in cloud albedo from cloud thinning. The mean change over the Arica Bight region, defined by the box in Fig. 2, is 20 W m^{-2} , or an approximately 15% increase in the regional-mean cloud albedo. Further south, the increase in cloud fraction over the Chilean coastal jet for the MAX N_d composite corresponds with an increase of approximately 50 W m^{-2} in the top-of-atmosphere shortwave fluxes, but over a region with small mean cloud fraction. The most dramatic changes in the fluxes are observed away from Arica Bight along 85°W, however, and are

primarily associated with cloud fraction differences, with only small changes in the cloud droplet numbers.

3.2. Radiosonde

Antofagasta (23.43°S, 70.43°W) is near the location of maximum N_d variability (Fig. 1) and composite changes in the satellite-derived cloud properties are representative of those for the Arica Bight region (Fig. 2). Composites of radiosondes from Antofagasta (1200 UTC or 0800 LT) help us interpret the satellite composites (Fig. 6). These show a strengthening of the inversion temperature for the MAX N_d composite (Fig. 6a, solid black line), with the MAX N_d radiosonde composite possessing a warmer and drier free troposphere than the MIN N_d composite (solid gray line). Composite differences in boundary-layer moisture and in the zonal wind are small and not necessarily significant.

The corresponding Reanalysis profiles, shown for a location approximately 500 km offshore Antofagasta, depict the boundary layer weakly. The vertical placement of the temperature and moisture inversion is approximately correct, but the underestimate of the inversion strength is pronounced, and the zonal winds not captured well. In contrast to the temperature and moisture Reanalysis composite profiles, the sense of the change between the MAX and MIN Reanalysis N_d zonal wind composites differs from the radiosonde composites. In one important feature, however, the Reanalysis agrees with the radiosondes: the MAX N_d Reanalysis composite also depicts a warmer and drier free troposphere than the MIN N_d Reanalysis composite. This is difficult to explain other than as increased free-tropospheric subsidence for the MAX N_d cases.

4. Regional Circulation

The spatial structure of the 850 hPa anomaly fields (geopotential height, subsidence and winds) is shown explicitly for the two composites in Fig. 7. The MAX N_d composite is characterized by weaker subsidence offshore (negative anomalies in dp/dt , blue color), an anomalous trough (contours) west of 85°W, and northerly winds. In contrast, the MIN- N_d composite presents an anomalous ridge and enhanced offshore subsidence. This pattern is

consistent with the changes in the climatological anticyclone shown in Fig. 5b, and the subsidence changes suggested at Antofagasta in Fig. 6.

The important meteorological parameters governing stratocumulus cloud behavior at daily/synoptic time scales are not well-established (e.g., Klein, 1997; Zhang et al., 2009), although lower tropospheric stability suggests itself as a sensible proxy (e.g., Mauger and Norris, 2007; Matsui et al., 2006). We first evaluated the applicability of static stability as a proxy for cloud cover at daily/synoptic timescales. The static stability defined as the difference between potential temperature (θ) at 850 hPa and 1000 hPa, was found to correlate better with MODIS cloud fraction than $\theta_{700\text{hPa}} - \theta_{1000\text{hPa}}$. A spatial map of the correlation at daily time scales between $\theta_{850\text{hPa}} - \theta_{1000\text{hPa}}$ and MODIS cloud fraction (Fig. 8) shows the highest positive correlation at 85°W and 25°S ($r = 0.55$), higher than that reported for the northeast Pacific at 30°N, 140°W using $\theta_{700\text{hPa}} - \theta_{\text{surface}}$ ($r=0.22$; Klein, 1997). The correlation is insignificant over the Arica Bight, expected based on Fig. 6.

Fig. 9 shows mean values of $\theta_{850\text{hPa}} - \theta_{1000\text{hPa}}$ (contours) along with the composite differences (colors). The largest static stability difference between the two composites occurs near the southern boundary of the stratocumulus deck, at approximately 30°S, 75-77°W, near if slightly east of the highest composite differences in cloud fraction (Fig. 6e). The stability changes are large in the same general area where the correlation between cloud fraction and static stability is high (Fig. 8), rationalizing the choice of NCEP-defined static stability as a proxy for cloud fraction at daily timescales.

At short timescales, the static stability variability is governed by the variability in $\theta_{850\text{hPa}}$ rather than near-surface, and we can explore its relationship to the other meteorological fields through a one-point linear correlation analysis that does not rely on the N_d compositing. The 850 hPa potential temperature time series at 20°S and 75°W serves as the reference point (Fig. 10 filled square; note this is approximately 300 km west of the Twin Otter point Alpha destination during VOCALS-REx) and is correlated with the 850 hPa geopotential height, subsidence and wind field time series at all other reanalysis grid points in Fig. 10. The one-point correlation analysis reveals an increase in the reference 850 hPa temperature is associated with a local increase in anomalous northerly winds

(actually a weakening of the southerly winds), as well as increases in the 850 hPa geopotential height further west between 75°-85°W. The relationship of the geopotential height anomaly field to the anomaly winds and subsidence are those of an anomalous trough to the west of South America. Fig. 10 suggests synoptic changes in the southeast Pacific stratocumulus deck reflect mid-latitude intrusions rather than equatorial intrusions. An example of the opposite behavior is discussed in Wyant et al. (2010) for mid-October, 2006, when enhanced southerly winds above the inversion corresponded to a decrease in cloud coverage and increase in a boundary-layer deepening at 85°W, 20°S. At the reference point in Fig. 10, increases in the 850 hPa geopotential height to its west are associated with a local weakening of the southerly 850 hPa winds, reducing free tropospheric cold temperature advection, and allowing the 850 hPa temperature to rise. Drawing on Fig. 8, the elevated static stability corresponds to an increase in cloud cover.

Perhaps counterintuitively, the increased cloud coverage at 85°W during the MAX- N_d composite is associated with weaker subsidence further offshore and increased subsidence at point Alpha (20°S and 72°W) and near the coast. The increase in free-tropospheric subsidence near the coast is consistent with the radiosondes at Antofagasta. While an increased subsidence-decreased cloud fraction relationship is not necessarily surprising at short time scales (e.g., Zhang et al., 2009; Mauger and Norris, 2010), it does run counter to intuition built from monthly-mean analyses (e.g., Bony and Dufresne, 2005).

Warmer temperatures during the MAX N_d composite relative to the MIN N_d composite extend fully throughout the troposphere within the NCEP Reanalysis (not shown), indicating a quasi-barotropic structure with an anomalous anticyclonic circulation. The stronger coastal subsidence during MAX N_d cases north of 25°S are reminiscent of the shallow, warm-core-low pressure cells of one-three day duration known as coastal lows (e.g., Garreaud et al., 2002; Garreaud and Rutllant, 2003). However, a coastal trough in sea level pressure is not apparent in our MAX N_d composite (Fig. 5a and b), the easterlies at Antofagasta remain weak in comparison to the coastal-low easterlies identified in Huneus et al. (2006), and the region south of 25°S is marked by an increase in cloud coverage, rather than a decrease. In addition, although more of our MIN N_d episodes last

only one day compared to the MAX N_d cases, the number of episodes lasting three or more days is the same for both composites (five) – longer than for typical coastal low events. Nevertheless, our high/low N_d composites in some ways resemble the ending/leading edge of coastal lows, and the common occurrence of both suggests there must be some common associations.

In contrast to coastal lows, cutoff-lows are upper-level low pressure centers with a quasi-barotropic structure (e.g., Fuenzalida et al., 2005) and thus seem similar to our MIN N_d composite. In addition, cutoff-lows can be preceded by quasi-stationary ridging reminiscent of our MAX N_d composite, with a duration exceeding that of the coastal lows. Cutoff-lows could be considered more intense manifestations of the upper-tropospheric potential vorticity perturbations identified through our composites. Although beyond the scope of the current work, the connection between cut-off lows and cloud property composites seems worthy of further investigation.

Previous studies have associated weaker surface winds at 33°S and 73°W with reduced cold surface temperature advection, in turn reducing cloud liquid water path and cloud fraction north of 20°S (Xu et al., 2004; Muñoz and Garreaud 2005; Wood et al., 2008). This contrasts with our finding that weaker alongshore winds co-occur with an increase in offshore cloud cover. The explanation may lie in our greater focus on submonthly synoptic activity and analysis of only October months, whereas the previous studies examined longer time spans that probably also captured seasonal changes. Our compositing appears to preferentially select for lifestages of mid-latitude baroclinic waves intruding upon the stratocumulus deck.

5. Precipitation Characteristics

Precipitation characteristics of the two composites were investigated using CloudSat reflectivity-height distributions constructed for a coastal and an offshore location. The coastal region encompasses 17°-27°S and 70°-80°W, an area slightly broader than the Arica Bight. The MAX N_d reflectivity-height distribution is narrower, centered near -25 dBZ and 1000 m, than the MIN N_d distribution (Fig. 11 a and b). For both composites, however, the most frequently occurring reflectivities are around -25 dBZ with heights

between 800 m and 1200 m. Few pixels have reflectivities > 0 dBZ, equivalent to a cloudbase rain rate of ~ 2 mm day⁻¹ (Comstock et al., 2004). Approximately one-sixth and one-third of the MAX/MIN N_d pixels exceed -17 dBZ (Table 1), equivalent to a cloudbase rainrate of 0.01 mm day⁻¹. The low radar reflectivities for both composites near the coast can be expected from the thin mean coastal cloud depths (Fig. 5d, contours). The slightly higher reflectivity values for the MIN N_d distribution are consistent with the deeper clouds and higher cloud tops and do indicate some drizzle, but for the MAX N_d distribution, hypotheses for cloud thinning based on depletion through precipitation seem discouraged (by the lack of observed precipitation). For the coastal clouds, little cloud thinning from precipitation is anticipated, based on previous work that clouds do not become sub-adiabatic until liquid water paths reach ~ 150 g/m³ and the frequency of occurrence of cloud radar reflectivities > 0 dBZ reaches 20% (Zuidema et al. 2005; Fig. 10). This finding will need to be modified for coastal conditions, however, to account for higher N_d and stronger cloud top entrainment.

The offshore CloudSat reflectivity-height distribution was constructed for the offshore region with the most pronounced change in cloud fraction between the two composites, defined by 20°-30°S and 80°-90°W (Fig. 11 panels c and d). A greater percentage of the offshore pixels were precipitating (reflectivities higher than -17 dBZ), consistent with Leon et al. (2008). The substantial increase in offshore cloud fraction for the MAX N_d composite is associated with only a slight shift towards lower radar reflectivities (Table 1). In addition, the percentage of pixels > 0 dBZ is approximately the same for both offshore composites. In addition, we note the minor change in cloud top height between the offshore MAX and MIN N_d composites, in spite of the large change in large fraction. This is consistent with some cancelling in the vertical and horizontal temperature advectations (i.e. less subsidence but also less free-tropospheric horizontal cold temperature advection).

6. Conclusions and Discussion

We have applied satellite retrievals to understand how synoptic conditions can change cloud droplet number concentrations. We focused on October months only, to reduce influences from the seasonal cycle. A one-year evaluation of the seasonal cycle in

cloudiness at San Felix Island (26S, 80W), located near the region with the largest cloud fraction changes (Fig. 5e), also found large variations in cloud cover and mesoscale cellular structure for this month, which has weaker baroclinicity than June-September but more pronounced baroclinicity than Dec.-March (Painemal et al., 2010). Comparisons between ship-based and MODIS-derived cloud depth estimates (see Appendix), and of ship-based aerosol concentration to MODIS-derived N_d values establish faith in the satellite retrievals and suggest the aerosol present are readily activated.

Episodes with high N_d over the Arica Bight are associated with a weaker anticyclone, weaker surface and free-tropospheric winds, and thinner clouds, also shown by Wood et al. (2008) and George and Wood (2010). We also find higher cloud droplet numbers are associated with more stable atmospheres, similar to Mauger and Norris (2007) and Matsui et al. (2006). In addition, we show that higher N_d values over the Arica Bight are concurrent with lower cloud top heights along with stronger inversion temperatures at Antofagasta (Fig. 6). Smaller differences in N_d occur near 18°S, where the wind speeds are smaller and less variable, allowing aerosols to stagnate. Changes in top-of-atmosphere shortwave fluxes show a spatial gradient, with thinner clouds near the coast dominating a reduction in shortwave reflectance, while 400 km offshore, the increase in cloud droplet number accounts for a slight increase in shortwave reflectance (Fig. 5f).

Changes in the easterlies (from radiosondes) at Antofagasta are not significant between the MAX and MIN N_d composites, and do not suggest significant changes in advection of continental aerosols to the stratocumulus deck. In addition, the stronger inversion and thinner clouds associated with larger N_d along the coast would discourage entrainment of free-tropospheric aerosols. MAX N_d days often occur in 2-4 days groups, during which the enhanced stability furthers multi-day aerosol transport within the boundary layer from the south, in evidence in Wood et al. (2008). This also allows high N_d conditions to correlate well with enhanced stability from previous days, similar to Mauger and Norris (2007).

Huneus et al. (2006) analyzed strong easterly events at Antofagasta (700 hPa zonal winds $> 5 \text{ m s}^{-1}$) during austral winter, finding a connection between one episode of upper-level easterlies and the increase of N_d . This suggested a connection to two important copper smelters, Chuquicamata (22.3°S, 68.9°W) and Potrerillos (26.4°S,

69.5°W), that are both above the boundary layer (2700 m and 2850 m a.s.l. respectively). In this study we did not find any event with easterly winds of that magnitude; possibly they are sporadic during austral spring when the midlatitude weather disturbances are less intense.

Approximately one-fourth of potential daily cases were excluded because they did not satisfy our criteria for overcast conditions over the Arica Bight. Given that thinner clouds are associated with the high- N_d composite, the days with low cloud cover over the Arica Bight may be more likely to resemble the high- N_d cases. Further south, around 30°S, these days are associated with increased cloud cover, a deeper boundary layer and deeper clouds, and resemble the aftermath of the coastal lows described by Garreaud et al. (2002) and Garreaud and Rutllant (2003). The leading edge of the ~2 day coastal low events encourage conditions conducive to pollution trapping in Santiago, Chile (33.3°S, 70.5°W), as well as easterly winds capable of advecting aerosol-rich air out to sea. The synoptic conditions that encourage coastal lows are similar to those of our MIN N_d composites, though the coastal low troughing in sea level pressure is not as apparent in our composite sea level pressures (Fig. 5 a and b). Coastal lows must undoubtedly impact the southerly manifestation of the high/low N_d composites discussed here.

Further offshore along 85°W, a large increase in cloud fraction and top-of-atmosphere shortwave fluxes is evident in the MAX N_d composite. This is synoptic, driven by mid-latitude baroclinicity rather than from the equator. As revealed in the anomalies at 850 hPa (Fig. 7) and the one-point correlation map (Fig. 10), an anomalously warm 850 hPa temperature near the coast is associated with an offshore trough-like pattern that enhances coastal subsidence but encourages anomalous free-tropospheric ascent offshore. Anomalous northerly winds along 85°W allow the above-inversion temperature to increase and increase the static stability, which is well-correlated with cloud fraction at this location. A similar synoptic episode is discussed in Wyant et al. (2010), but with a reduction of offshore cloud fraction associated with a deeper boundary layer and stronger southerlies. It is also useful to note that the increased cloud cover is associated with decreased subsidence. Yet, as is apparent in Fig. 5, the increased cloud cover is associated with widespread decreases in cloud top height, because the anomalous horizontal warm temperature advection above the inversion is more than compensating

for the decrease in subsidence,. Numerical simulations during VOCALS-REx period (October-November 2008) indicate that the horizontal advection of the marine boundary layer height is larger than the vertical velocity at the top of the boundary layer, stressing the importance of the changes in the southerly winds over the subsidence (Rahn and Garreaud, 2010). The most significant features of the circulations associated with the two composites are highlighted in a schematic (Fig. 13).

An offshore albedo increase from the increase in cloud cover, along with an albedo decrease from near-coastal cloud thinning, means that a spatial gradient in albedo along 20°S will be difficult to detect in some VOCALS-REx aircraft flights (e.g., Twohy et al., 2010). Since several of the MAX/MIN cases occurred within a day of VOCALS-REx C-130 flights (see Fig. 12), our analysis can provide context for the VOCALS-REx observations. Our Oct. 2008 MAX N_d cases ended when a mid-latitude trough moved through the region, while the Oct. 2008 MIN N_d cases loosely coincided with baroclinic troughs (Rahn and Garreaud, 2010). The LWP- N_d correlation over the Arica Bight was negative ($r = -0.27$), as expected, but contained significant day-to-day variability that can mask the correlation evident within a larger data sample. This explains a positive LWP- N_d correlation observed in Twin Otter VOCALS-Rex measurements at Point Alpha (75W, 20S; Bruce Albrecht and Xue Zheng, pers. comm.).

Several avenues for further work present themselves. The implications of our data for albedo susceptibility $d(A)/d(N_d)$ still need to be assessed. Since both satellite cloud top height and inversion temperature indicate less favorable conditions for aerosol entrainment during MAX N_d , we speculate that the main source of anthropogenic aerosols must be situated within the boundary layer. This hypothesis implies the contribution of several sources alongshore and perhaps includes non-point-source pollution that has been brought out to sea, more likely from the more developed southern region of Chile (see also George and Wood, 2010). The poor reanalysis representation of the Chile-Peru coastline discouraged us from using back-trajectories to study the time history of cloud parcels, however (e.g., Mauger and Norris, 2007. New reanalyses (e.g., Year of Tropical Convection; ERA-Interim; NCEP Climate Forecast System Reanalysis

and Reforecast) with better resolution of the orography and of the physical processes will allow for more confident investigations of near-coastal aerosol-cloud interactions. Further investigation of the connection of our composites to the synoptic climatology of the southeast Pacific will also help us better determine the impact of future climates upon this region, arguably the largest subtropical stratocumulus deck on the planet.

Acknowledgements

Funding support from the NOAA Climate Prediction Program for the Americas (Grant NA06OAR4310056) and from the National Science Foundation (Grant ATM-0745470) is gratefully acknowledged. We thank Joel Norris and two anonymous reviewers for their careful reading of the manuscript.

Appendix: Error Analysis and Ship-satellite comparisons

Instantaneous swath data (level 2) from both the Terra and Aqua platforms (~1030 LT and ~1330 LT overpasses, respectively) were used for the validation comparisons to *in situ* observations. H_{sat} and N_d derived from instantaneous level 2 data were spatially averaged over an area of 25 km by 25 km, corresponding to a 7 m s^{-1} “frozen turbulence” advective speed over one hour. For overcast, opaque, mostly unbroken, warm cloud pixels, the a priori error in H_{sat} (25 km² scale) from a τ error of 8% (Bennartz, 2007) and a conservative r_e (2.1 micron) error of ~20% is ~11% (Marshak et al. 2006). The error in N_d will be dominated by the error in the MODIS-derived effective radius through the $r_e^{-5/2}$ dependence, which can account for a 50% error in N_d alone. This encourages us to consider the sources for effective radius error more closely. The effective radius retrieval is most suspect in broken cloud conditions, where r_e can be systematically overestimated (e.g., Marshak et al., 2006). We observed that low N_d values tended to be associated with high-LWP clouds (not shown), which are more likely to precipitate, and which corresponded poorly to the surface-based aerosol measurements for the lower values of N_d . This suggested the presence of cloud inhomogeneities, whose impact upon the N_d retrieval we attempted to minimize by limiting our quantitative analysis to N_d values $> 50 \text{ cm}^{-3}$ for overcast pixels. In addition, averaging to a scale of 25 km² allows for

compensation of the largest three-dimensional radiative transfer effects within individual pixels. If we assume an r_e (2.1 micron) error of 10% based on comparisons to microwave-derived r_e (Bennartz, 2007, Fig. 4), we estimate a N_d error of 26% (also accounting for uncertainty in our assumed Γ_{ad}). This is less conservative than the uncertainty estimate of 50% within Bennartz (2007), but seems justified for our more restricted, regional dataset.

The validation comparisons draw on a more comprehensive database of *in situ* observations from six NOAA cruises (October, 2001, 2005, 2006, 2007, and November, 2003 and December, 2004). The ship-based aerosol number concentration N_a is a direct measurement, typically made from a Particle Measuring System Lasair-II instrument, which measures all particles greater than 0.1 microns, but does not control for humidity. For the 2004 cruise, data from a Differential Mobility Analyser are used (Tomlinson et al., 2007). Aerosol counts gathered from both instruments during the 2003 cruise show good agreement (Tomlinson et al. 2007). The ship-based cloud depth (H_{ship}) is computed as the difference between the radiosonde inversion base height (placed at the temperature minimum; radiosondes were launched at either 4 or 6 hour intervals) and hourly-averaged ceilometer cloud base heights. Comparisons were restricted to the one-hour time periods spanning the radiosondes.

H_{sat} and H_{ship} values correlate well with each other ($r=0.54$), increasing to 0.7 when restricting the sample to $H_{ship} < 400$ m and to overcast periods (ceilometer hourly cloud fractions $> 90\%$) (Fig. 14a; only overcast periods are shown). H_{sat} values often exceed H_{ship} , with a mean bias of 59 m for $H_{ship} < 400$ m. Schuller et al. (2003) found a similar bias between remote sensed and in-situ cloud depth; an explanation is currently lacking though an unexplained MODIS r_e overestimate (Bennartz, 2007; Marshak et al., 2006) is one possibility.

Satellite-derived N_d are compared to ship-based aerosol concentrations (size > 0.1 micron) in Fig. 14b, with no constraint placed on the hourly ceilometer cloud fractions towards increasing the data sample. Most of the aerosol concentration measurements were taken near $85^\circ W$ and $20^\circ S$, with a limited sampling near the coast. N_d and N_a show an obvious correlation ($r=0.65$, increasing to 0.8 for hourly-mean ceilometer cloud fractions > 0.9), with N_d typically $< N_a$, demonstrating physical consistency. The values

of both N_d and N_a are higher when sampled closer to the coast (east of 80°W, black filled circles in Fig. 1b).

A quantitative assessment of the observed N_d - N_a relationship can be expressed through an aerosol cloud index $\frac{d \ln N_d}{d \ln N_a}$ (McComiskey et al., 2009). Such observed relationships

have been compared to climate model values (e.g., Quaas et al., 2009) and additional care was taken to determine the best-fit line. The mean of the N_a standard deviations about the hourly-mean value was used as a mean N_a uncertainty estimate (10 cm⁻³) and a constant N_d error of 26%. We restricted the data samples to $N_d > 50$ cm⁻³ as a proxy for non-precipitating clouds and to control for gross overestimates in the effective radius retrievals caused by cloud inhomogeneities. Taking both N_a and N_d uncertainty estimates into account, we find a best-fit value for $\frac{d \ln N_d}{d \ln N_a}$ of 0.56 (York et al. 2004, but using

mean rather than individual datum uncertainties). For comparison, Pruppacher and Klett (1997) suggest a value of 0.7 for $\frac{d \ln N_d}{d \ln N_a}$ based on droplet activation theory, while

McComiskey et al. (2009) find an empirical value of 0.48 using cloud microphysical retrievals from surface-based remote sensors of marine stratocumulus clouds at Pt. Reyes, CA. Quaas et al. (2009) find a sensitivity of MODIS-derived N_d to the aerosol optical depth at Pt. Reyes that is close to the corresponding surface-based value.

Comparison to other published values of $\frac{d \ln N_d}{d \ln N_a}$ must take many factors into account.

McComiskey et al. (2009) document a strong reduction with increasing scale, for example, though satellite-derived values within Quaas et al. (2009) are similar to the surface-based value. Our value is therefore fairly high given the 25 km² scale. Moreover, 42% of our variation in N_d is explained by the aerosol concentration variability, compared to 15% for McComiskey et al. (2009). Some of the explanation is provided by Fig. 2, for which daily maps of Terra N_d and LWP values were averaged over the five October months. Many of the higher N_d values are associated with thinner clouds (LWP < 90 g/m², contours in Fig. 2) that are less likely to be drizzling (e.g., Leon et al., 2008) and more likely to be adiabatic if offshore (e.g., Zuidema et al., 2005). For such

clouds, values of $\frac{d \ln N_d}{d \ln N_a}$ are typically higher (McComiskey et al., 2009; Kim et al. 2008). Three-dimensional radiative transfer effects upon the r_e and thereby N_d retrieval, which will be more pronounced for thicker, more broken clouds with naturally higher r_e , may also contribute to a higher value for $\frac{d \ln N_d}{d \ln N_a}$ by artificially lowering low values of N_d even further, despite our efforts to screen for this.

References

Ackerman, A., Kirkpatrick, M., Stevens, D., and Toon, O.: The impact of humidity above stratiform clouds on indirect aerosol climate forcing. *Nature*, 432, pp. 1014-1017, 2004.

Albrecht, B.: Aerosol, clouds microphysics, and fractional cloudiness, *Science*, 245, 1227-1230, 1989.

Bennartz, R.: Global assessment of marine boundary layer cloud droplet number concentration from satellite, *J. Geophys. Res.*, 112, D02201, doi:10.1029/2006JD007547, 2007.

Bony, S., and Dufresne, J.-L.: Marine boundary layer clouds at the heart of tropical cloud feedback uncertainties in climate models. *Geophys. Res. Lett.*, 32, L20806, doi:10.1029/2005GL023851, 2005.

Borg, L., A., and Bennartz R.: Vertical structure of stratiform marine boundary layer clouds and its impact on cloud albedo, *Geophys. Res. Lett.*, 34, L05807, doi:10.1029/2006GL028713, 2007.

Brenguier, J. L., Pawlowska, H., Schüller, L., Preusker, R., Fischer, J., and Fouquart, Y.: Radiative properties of boundary layer clouds: Droplet effective radius versus number concentration, *J. Atmos. Sci.*, 57, 803–821, 2000.

Brenguier J.-L., Pawlowska, H., and Schüller, L.: Cloud microphysical and radiative properties for parameterization and satellite monitoring of the indirect effect of aerosol on climate, *J. Geophys. Res.*, 108 (D15), 8632, doi:10.1029/2002JD002682, 2003.

Bretherton, C. S., Uttal, T., Fairall, C. W., Yuter, S., Weller, R., Baumgardner, D., Comstock, K., Wood, R., and Raga, G.: The EPIC 2001 stratocumulus study. *Bull. Amer. Meteor. Soc.*, 85, 967–977, 2004.

Christensen, M. W., Coakley, J. A., and Tahnk, W. R.: Morning-to-Afternoon evolution of marine stratus polluted by underlying ships: Implications for the relative lifetimes of polluted and unpolluted clouds. *J. Atmos. Sci.*, 66, pp. 2097-2106, 2009.

Comstock, K. K., Wood, R., Yuter, S. E., and Bretherton, C. S.: Reflectivity and rain rate in and below drizzling stratocumulus. *Q. J. R. Meteorol. Soc.*, 130, 2891-2918, 2004.

Comstock, K. K., Bretherton, C. S., and Yuter, S. E.: Mesoscale variability and drizzle in southeast Pacific stratocumulus. *J. Atmos. Sci.*, 62, 3792–3807, 2005.

Fuenzalida, H. A., Sanchez, R., and Garreaud, R. D.: A climatology of cutoff lows in the Southern Hemisphere. *J. Geophys. Res.*, 110, D18101, doi: 10.1029/2005JD005934, 2005.

Garreaud, R., Rutllant, J., and Fuenzalida, H.: Coastal lows along the subtropical west coast of south America: Mean structure and evolution. *Mon. Wea. Rev.*, 130, 75-88, 2002.

Garreaud, R., and Rutllant, J.: Coastal lows along the subtropical west coast of south America: Numerical simulation of a typical case. *Mon. Wea. Rev.*, 131, 891-908, 2003.

George, R. and R. Wood: Subseasonal variability of low cloud radiative properties over the southeast Pacific Ocean. *Atmos. Chem. Phys. Discuss.*, 9, pp. 25275-25321, 2009.

Han, Q., Rossow, W. B, Zeng, J., and Welch, R.: Three different behaviors of liquid water path of water clouds in aerosol-cloud interactions. *J. Atmos. Sci.*, 59, 726-735, 2002.

Hartmann, D. L., Ockert-Bell, M. E., and Michelsen, M. L.: The effect of cloud type on Earth's balance: Global analysis. *J. Climate*, 5, 1281-1304, 1992.

Hawkins, L. N., Russell, L. M., Covert, D. S., Quinn, P. K., and Bates, T. S.: Carboxylic acids, sulfates, and organosulfates in processed continental organic aerosols over the southeast Pacific ocean during VOCALS-Rex 2008. *J. Geophys. Res.*, doi:10.1029/2009JD013276, 2010.

Huneeus N., Gallardo, L., and Rutllant, J. A.: Offshore transport episodes of anthropogenic sulfur in northern Chile: Potential impact on the stratocumulus cloud deck, *Geophys. Res. Lett.*, 33, L19819, doi:10.1029/2006GL026921, 2006.

Jiang H., Feingold, G., and Cotton, W. R.: Simulations of aerosol-cloud-dynamical feedbacks resulting from entrainment of aerosol into the marine boundary layer during the Atlantic Stratocumulus Transition Experiment, *J. Geophys. Res.*, 107 (D24), 4813, doi:10.1029/2001JD001502, 2002.

Kalnay, E., Kanamitsu, K., Kistler, R., et al: The NCEP/NCAR 40-years Reanalysis project. *Bull. of Amer. Meteor. Soc.*, 77, 437-471, 1996.

Kato, S., and A. Marshak: Solar zenith and viewing geometry-dependent errors in satellite retrieved cloud optical thickness: Marine stratocumulus case. *J. Geophys. Res.*, 114, doi:10.1029/2008JD010579, 2009

Kim B.-G., Miller, M. A., Schwartz, S. E., Liu, Y., and Min, Q.: The role of adiabaticity in the aerosol first indirect effect, *J. Geophys. Res.*, 113, D05210, doi:10.1029/2007JD008961, 2008.

Klein, S. A., and Hartmann, D. L.: The seasonal cycle of low stratiform clouds. *J. Climate*, 6, 1587-1606, 1993.

Klein, S. A.: Synoptic variability of low-cloud properties and meteorological parameters in the subtropical trade wind boundary layer. *J. Climate*, 10, 2018-2039, 1997.

Kubar, T., Hartmann, D. L. and Wood, R.: Understanding the importance of microphysics for warm rain in marine low clouds: Part I. Satellite observations. *J. Atmos. Sci.*, 66, 2953-2972, 2009.

Leon D. C., Wang, Z. and Liu, D.: Climatology of drizzle in marine boundary layer clouds based on 1 year of data from CloudSat and Cloud-Aerosol Lidar and Infrared Pathfinder Satellite Observations (CALIPSO), *J. Geophys. Res.*, 113, D00A14, doi:10.1029/2008JD009835, 2008.

Loeb, N., and Schuster, G.: An observational study of the relationship between cloud, aerosol and meteorology in broken low-level cloud conditions. *J. Geophys. Res.*, 113, D14214, doi: 10.1029/2007JD009763, 2008.

Marshak, A., Platnick, S., Varnai, T., Wen, G., and Cahalan, R. F.: Impact of 3D radiative effects on satellite retrievals of cloud droplet sizes. *J. Geophys. Res.*, 111, D09207, doi: 10.1029/2005JD006686, 2006.

Martin G. M., Johnson, D. W., and Spice A.: The measurement and parameterization of effective radius of droplets in warm stratocumulus clouds. *J. Atmos. Sci.*, **51**, 1823–1842, 1994

Matsui T., Masunaga, H., Kreidenweis, S. M., Pielke, Sr, R. A., Tao, W.-K., Chin, M., and Kaufman, Y. J.: Satellite-based assessment of marine low cloud variability associated with aerosol, atmospheric stability, and the diurnal cycle, *J. Geophys. Res.*, 111, D17204, doi:10.1029/2005JD006097, 2006.

Mauger G. S., and Norris J. R.: Meteorological bias in satellite estimates of aerosol-cloud relationships, *Geophys. Res. Lett.*, 34, L16824, doi:10.1029/2007GL029952, 2007.

Mauger, G.S. and Norris, J. R.: Assessing the impact of meteorological history on subtropical cloud fraction. *J. Climate*, in press.

McComiskey A., Feingold, G., Frisch, A. S., Turner, D. D., Miller, M. A., Chiu, J. C., Min, Q., and Ogren, J. A.: An assessment of aerosol-cloud interactions in marine stratus clouds based on surface remote sensing, *J. Geophys. Res.*, 114, D09203, doi:10.1029/2008JD011006, 2009.

Muñoz, R., and Garreaud, R.: Dynamics of the low-level jet off the coast of subtropical South America. *Mon. Wea. Rev.*, 133, 3661-3677, 2005.

Murphy, D. M., Solomon, S., Portmann, R. W., Roselof, K. H., Forster, P. M., and Wong, T.: An observationally based energy balance for the Earth system since 1950. *J. Geophys. Res.*, 114, D17107, doi:10.1029/2009JD012105, 2009.

Painemal, D., Garreaud, R., Rutllant, J. and Zuidema, P.: Southeast Pacific stratus: High-frequency variability and mesoscale structures over San Felix Island. *J. Appl. Meteor. Clim.*, Vol. 49, No. 3, 463–477, 2010.

Platnick, S., King, M., Ackerman, S., Menzel, W., Baum, B., Riedi, J., and Frey, R.: The MODIS cloud products: Algorithms and examples from Terra. *IEEE Trans. Geosci. Remote Sens.*, 41, 459-473, 2003.

Pruppacher H. R., and Klett, J. D.: *Microphysics of Clouds and Precipitation*. Kluwer Academic, 954 pp, 1997.

Quaas, J., Ming, Y., Menon, S., Takemura, T., Wang, M., Penner, J. E., Gettelman, A., Lohmann, U., Bellouin, N., Boucher, O., Sayer, A. M., Thomas, G. E., McComiskey, A., Feingold, G., Hoose, C., Kristjánsson, J. E., Liu, X., Balkanski, Y., Donner, L. J., Ginoux, P. A., Stier, P., Feichter, J., Sednev, I., Bauer, S. E., Koch, D., Grainger, R. G., Kirkevåg, A., Iversen, T., Seland, Ø., Easter, R., Ghan, S. J., Rasch, P. J., Morrison, H.,

Lamarque, J.-F., Iacono, M. J., Kinne, S., and Schulz, M.: Aerosol indirect effects – general circulation model intercomparison and evaluation with satellite data, *Atmos. Chem. Phys. Discuss.*, 9, 12731–12779, 2009.

Rahn, D. and Garreaud, R.: Marine boundary layer over the subtropical southeast Pacific during VOCALS-Rex-Part 2: Synoptic variability, *Atmos. Chem. Phys. Discuss.*, 9, 26063–26094, 2010.

Randall, D. A. et al.: Climate models and their evaluations in *Climate Change 2007: The Physical Science Basis. Contribution of Working Group 1 to the Fourth Assessment Report of the Intergovernmental Panel on Climate Change*, edited by S. Solomon, pp. 589-662. Cambridge Univ. Press, Cambridge, U.K. 2007.

Schüller L., and Brenguier, J.-L., and Pawlowska, H.: Retrieval of microphysical, geometrical, and radiative properties of marine stratocumulus from remote sensing, *J. Geophys. Res.*, 108 (D15), 8631, doi:10.1029/2002JD002680, 2003.

Seethala, C., and Horváth, Á.: Global Assessment of AMSR-E and MODIS Cloud Liquid Water Path Retrievals in Warm Oceanic Clouds, *J. Geophys. Res.*, doi:10.1029/2009JD012662, 2010.

Stevens, B., and Feingold, G.: Untangling aerosol effects on clouds and precipitation in a buffered system. *Nature*, 461, 607-613, doi:10.1038, 2009.

Szczodrak, M., Austin, P. H., and Krummel, P. B.: Variability of optical depth and effective radius in marine stratocumulus clouds, *J. Atmos. Sci.*, 58, 2912-2926, 2001

Stephens G. L., Vane, D., G., Boain, R., J., et al.: The CloudSat mission and the A-Train: A new dimension of space-based observations of clouds and precipitation. *Bull. Amer. Meteor. Soc.*, 83, 1771–1790, 2002.

Tomlinson J. M., Li, R. and Collins, D. R.: Physical and chemical properties of the aerosol within the southeastern Pacific marine boundary layer, *J. Geophys. Res.*, 112, D12211, doi:10.1029/2006JD007771, 2007.

Twohy, C., A. Adams, P. Zuidema, D. Leon, R. George and R. Wood: Factors controlling the microphysical and radiative properties of stratocumulus clouds in the Southeast Pacific. *CLIVAR Exchanges*, 53, p. 22-25. 2010.

Twomey, S.: The influence of pollution on the shortwave albedo of clouds. *J. Atmos. Sci.*, 34, 1149-1152, 1977.

Wielicki B. A., Barkstrom, B. R., Harrison, E. F., Lee, III, R. B., Smith, G. L. and Cooper, J. E.: Clouds and the Earth's Radiant Energy System (CERES): An Earth Observing System Experiment. *Bull. Amer. Meteor. Soc.*, 77, 853–868, 1996.

Wood R., Comstock, K. K., Bretherton, C. S., Cornish, C., Tomlinson, J., Collins, D. R. and Fairall, C.: Open cellular structure in marine stratocumulus sheets, *J. Geophys. Res.*, 113, D12207, doi:10.1029/2007JD009371, 2008.

Wood R. and Mechoso, C. R.: Southeastern Pacific Coupled Climate Field Experiment. *EOS, Transactions American Geophysical Union*, VOL. 89, NO. 33, 303, doi:10.1029/2008EO330003, 2008.

Wyant, M. C., Wood, R., Bretherton, C. S., Mechoso, C. R., Bacmeister, J., Balmaseda, M. A., Barrett, B., Codron, F., Earnshaw, P., Fast, J., Hannay, C., Kaiser, J. W., Kitagawa, H., Klein, S. A., Khler, M., Manganello, J., Pan, H.-L., Sun, F., Wang, S., and Wang, Y.: The PreVOCA experiment: modeling the lower troposphere in the Southeast Pacific, *Atmos. Chem. Phys. Discuss.*, 9, 23909–23953, 2009.

Xu, H., Wang, Y. and Xie, S.-P.: Effects of the Andes on eastern Pacific climate: A regional atmospheric model study. *J. Climate*, 17, 589-602, 2004.

York, D., N. Evensen, M. L. Martinex and J. D.B. Delgado: Unified equations for the slope, intercept, and standard errors of the best straight line. *Am. J. Phys.*, 72, 2004.

Zhang, Y., Stevens, B., Medeiros, B. and Ghil, M.: Low-cloud fraction, lower-tropospheric stability and large-scale subsidence. *J. Climate*, 22, 4827-4844, 2009.

Zuidema, P., Westwater, E., Fairall, C. and Hazen, D.: Ship-based liquid water path estimates in marine stratocumulus. *J. Geophys. Res.*, 110, D20206, doi:10.1029/2005JD005833, 2005.

Zuidema, P., Painemal, D., de Szoeki, S. and Fairall, C.: Stratocumulus cloud top height estimates and their climatic implications. *J. Climate*, 22, 4652-4666, 2009.

Table 1. Number and percentage of CloudSat pixels below two km of height, at two separate regions, above two different reflectivity thresholds.

	Domain	dBZ \geq -17	dBZ > 0
MAX N_d	17° - 27°S and 70° - 80°W	973 pixels / 13.6 %	44 pixels / 0.6%
MIN N_d	17° - 27°S and 70° - 80°W	13611 pixels/ 37.4%	1168pixels / 3.2%
MAX N_d	20° - 30°S and 80° - 90°W	11596 pixels /43.9 %	2589 pixels / 9.8%
MIN N_d	20° - 30°S and 80° - 90°W	26006 pixels /55.4 %	4013 pixels / 8.5%

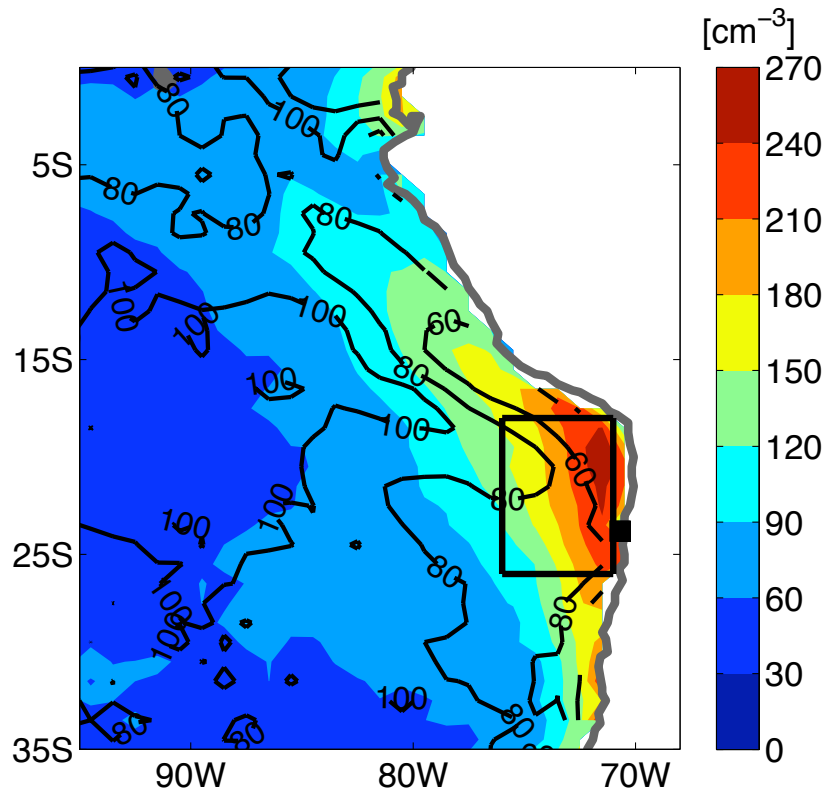


Figure 1. Mean N_d ($\# \text{ cm}^{-3}$, colors) and LWP (g m^{-2} , contours), based on October 2001 and 2005-2008 Terra daytime MODIS level 3 data. The box indicates the area over which the daily-mean N_d were averaged and the black square indicates Antofagasta.

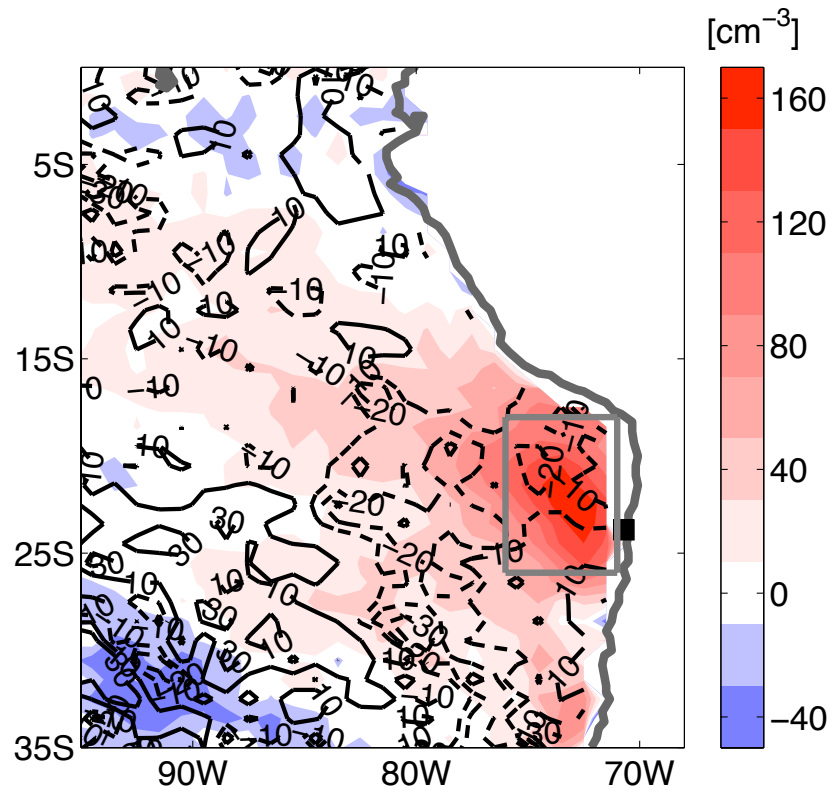


Figure 2. As Fig. 2 but for the MAX-MIN N_d composite differences: N_d (colors) and LWP (contours).

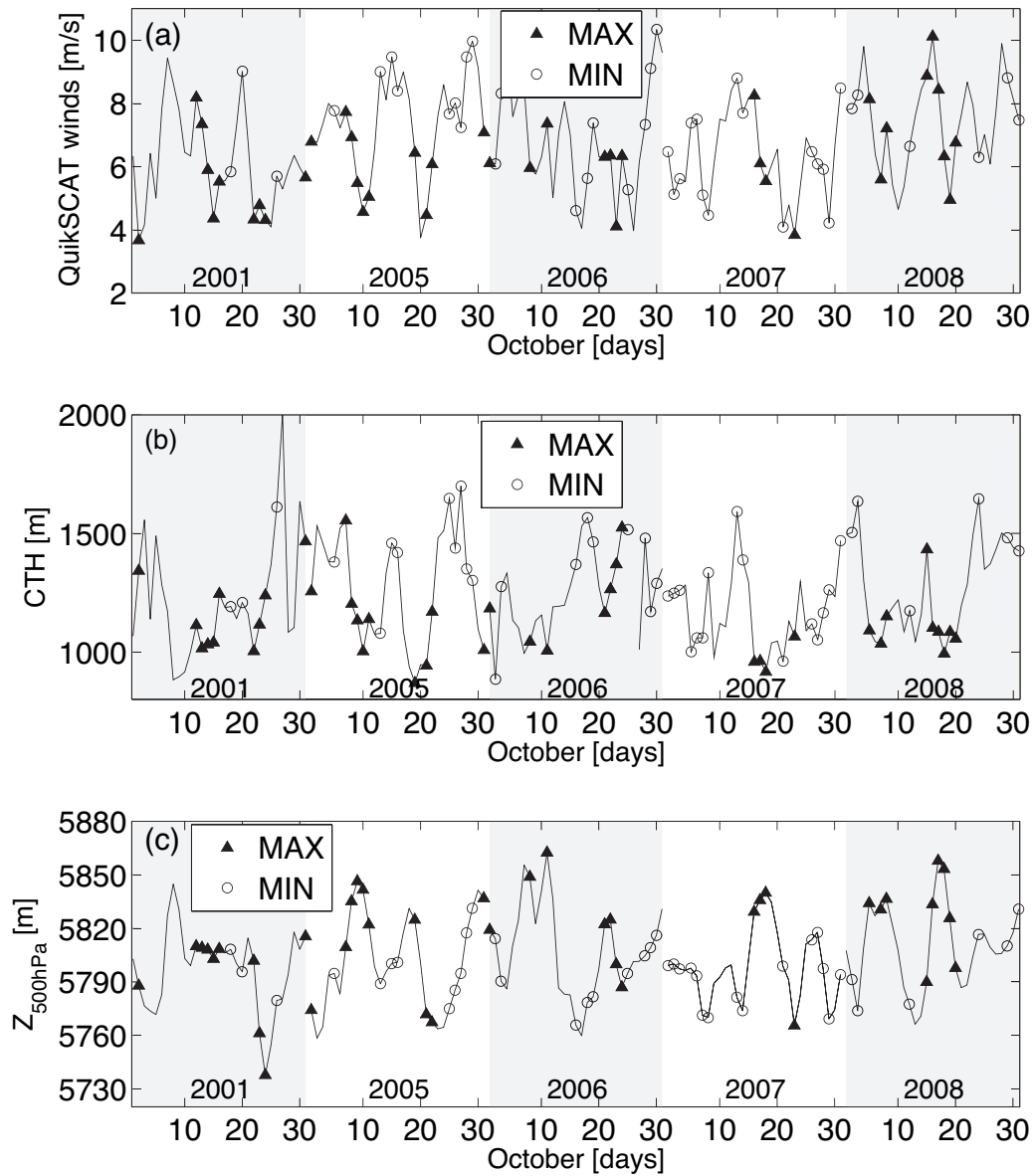


Figure 3. Time series of: a) mean surface winds (QuikSCAT) at 20°S - 30°S , 70°W - 90°W , b) mean Terra-daytime MODIS-derived cloud top heights at 20°S - 30°S , 70°W - 80°W and c) mean 500 hPa geopotential height at 15°S - 35°S , 70°W - 100°W . Black triangles and open circles correspond to MAX and MIN N_d days.

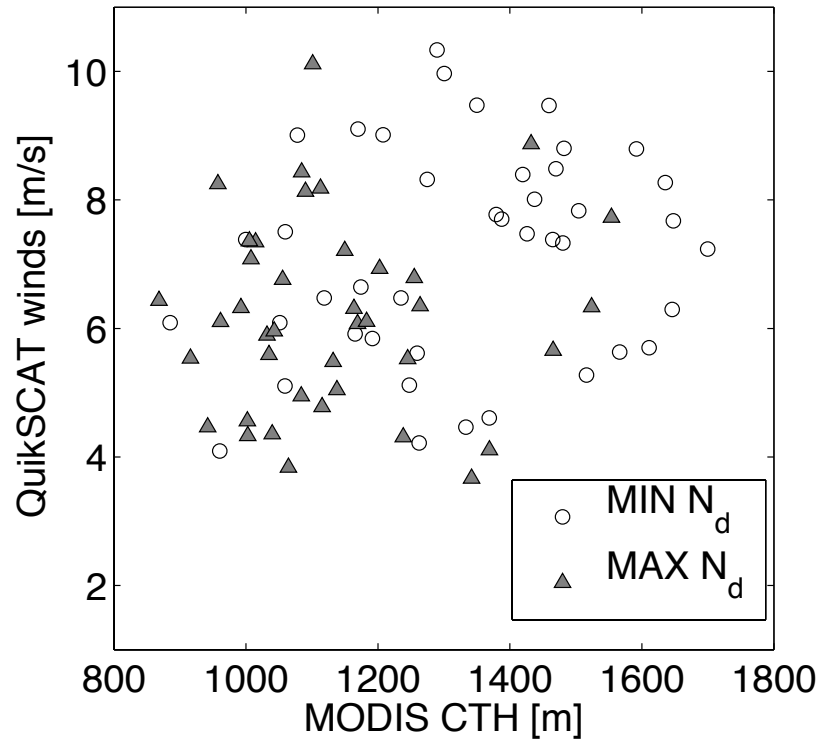


Figure 4. Scatterplot between Terra daytime MODIS-derived cloud top height and evening-pass QuikSCAT winds, taken from Fig. 4. Open circles and filled triangles correspond to MIN and MAX N_d days respectively.

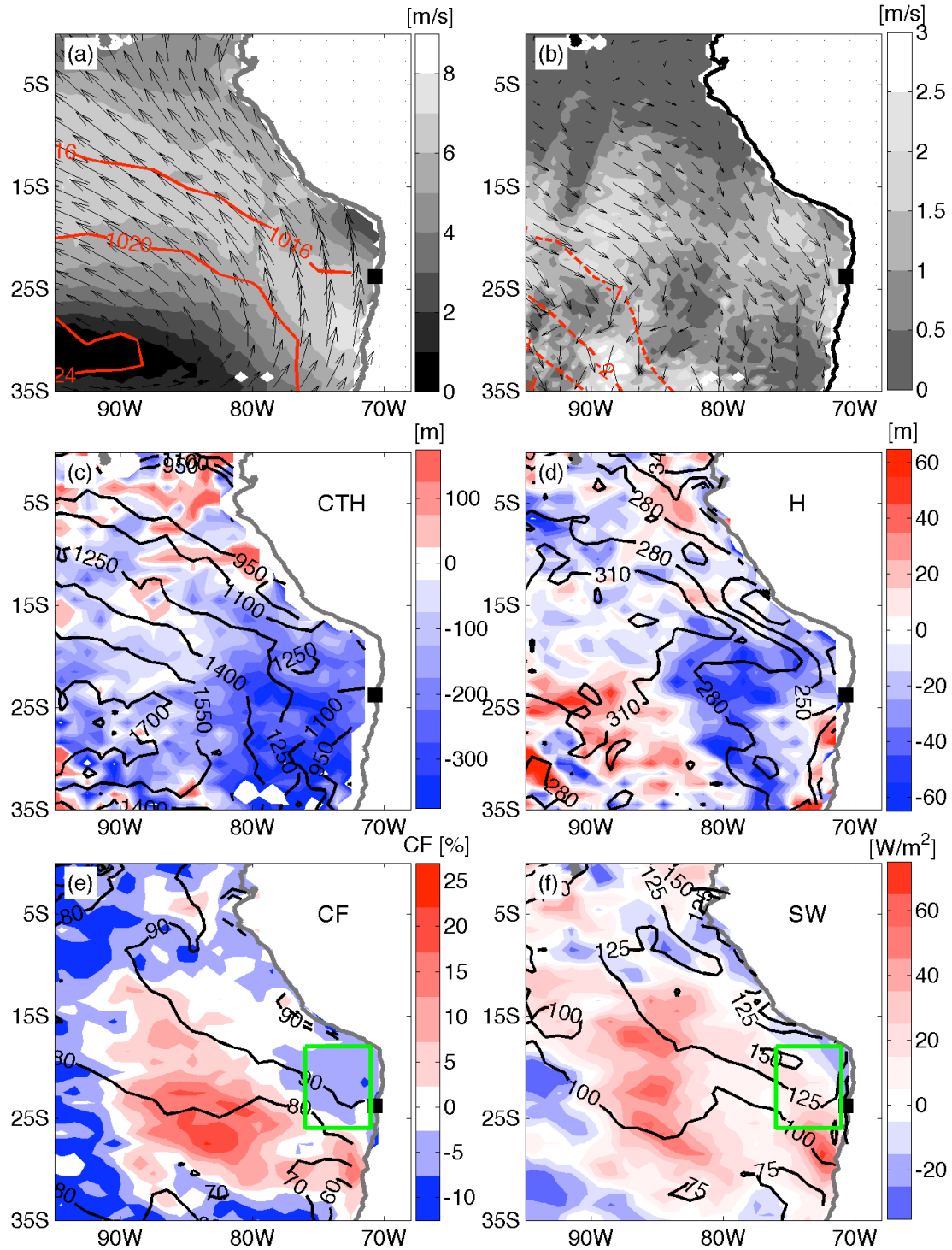


Figure 5. a) and b) MAX and MIN N_d composite NCEP sea level pressure (red contours), surface wind magnitude and direction (greyscale and arrows; QuikScat descending pass, 18LT). Mean (contours) and MAX-MIN composite difference (colors) in c) MODIS-derived cloud top height, d) MODIS-derived cloud depth, e) MODIS cloud fraction and

f) CERES top-of-atmosphere shortwave fluxes. All MODIS data is Terra daytime level 3. Location of Antofagasta indicated by black square, and Arica Bight domain is shown in Fig. 6 e and f.

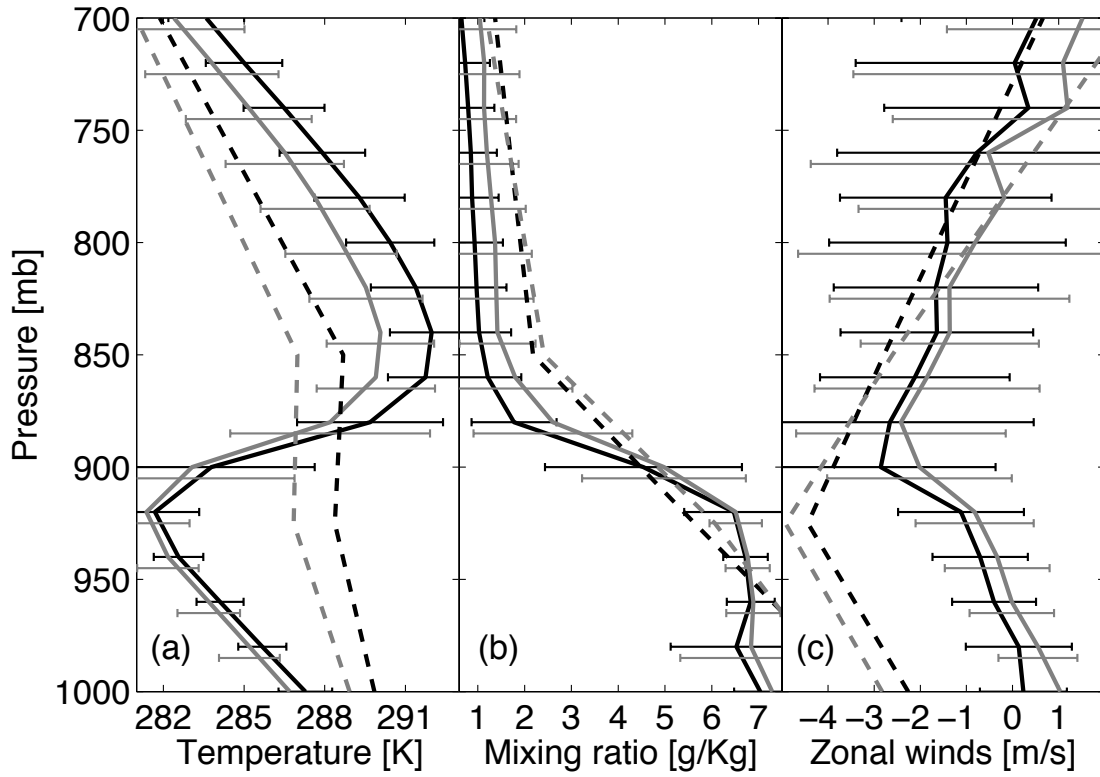


Figure 6. Antofagasta radiosonde (solid) and NCEP reanalysis (dashed) MAX- N_d (black) and MIN- N_d (grey) composites of a) temperature, b) mixing ratio, and c) zonal winds. Antofagasta (23.5°S , 70.5°W) radiosondes launched at 1200 UTC (0800 LT). NCEP-NCAR reanalysis data from 22.5°S , 75°W .

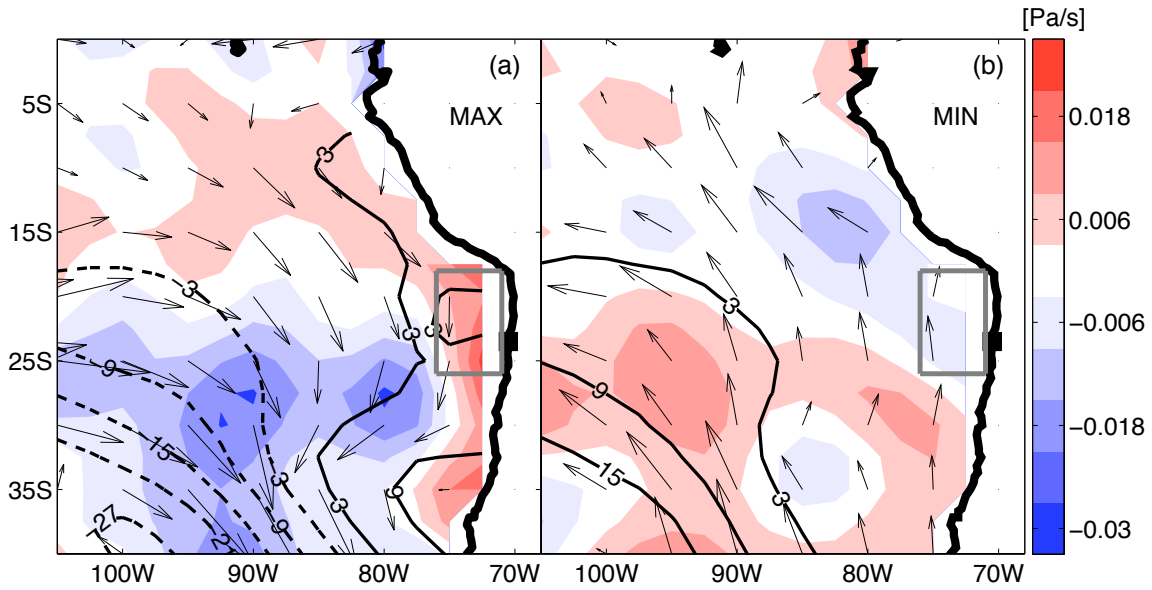


Figure 7. NCEP reanalysis anomalies at 850 hPa: Geopotential heights (contours), subsidence (dp/dt , colorscale), and winds, for (a) MAX N_d composite, (b) MIN N_d composite. Antofagasta location indicated with a black box, and Arica Bight domain contoured in grey.

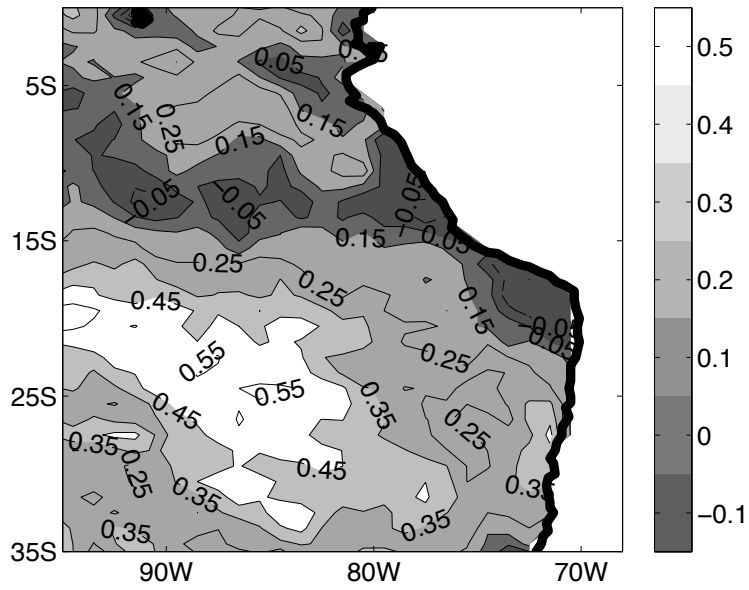


Figure 8. Linear correlation between October daytime Terra MODIS cloud fraction and daily-mean $\theta_{850\text{hPa}} - \theta_{1000\text{hPa}}$. Correlation values greater than 0.20 below 15° S pass the 99% significance level of a Student's t test.

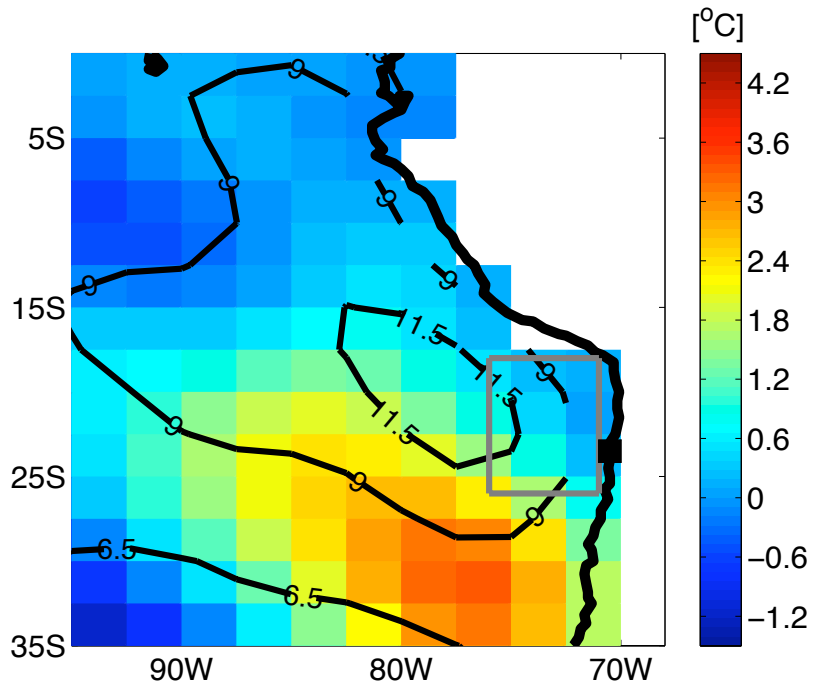


Figure 9. October-mean $\theta_{850\text{hPa}} - \theta_{1000\text{ hPa}}$ (contours) and MAX-MIN N_d composite differences in $\theta_{850\text{hPa}} - \theta_{1000\text{ hPa}}$ (color). Arica Bight domain contoured in grey.

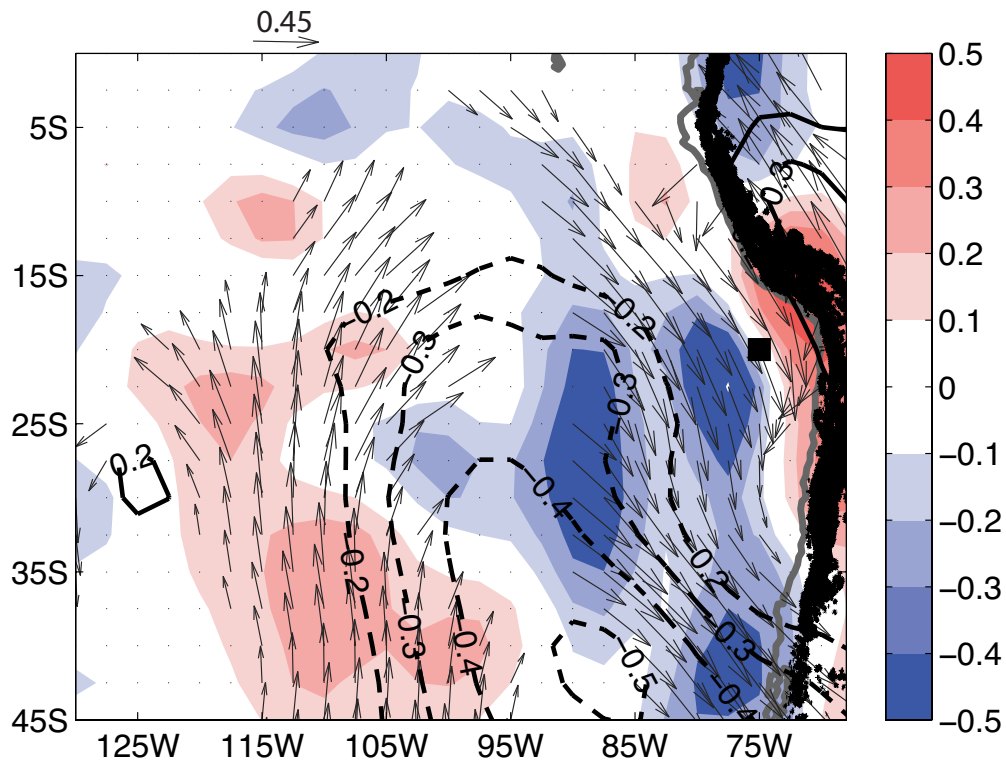


Figure 10. One point correlation between the potential temperature at 20°S and 75°W (square) and: subsidence (pressure velocity dp/dt , colors; positive values imply subsidence), geopotential height (contours) and wind (arrows), all at 850 hPa. Absolute values of correlation higher than 0.25 for the geopotential height and subsidence fields pass the 99% significance level of a Student's t test. The winds are only shown if the meridional component of the wind-temperature correlation is statistically significant. Topography higher than 1500 m is indicated by the black shade.

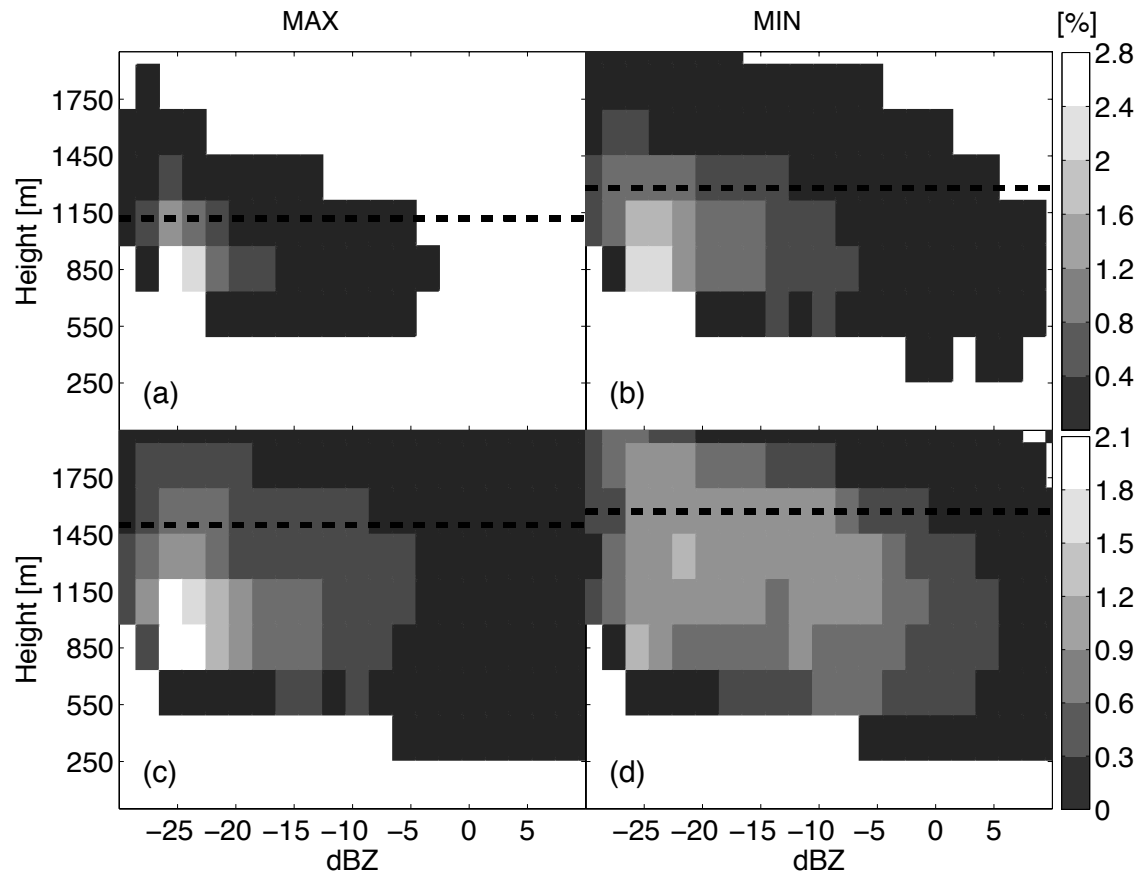


Figure 11. CloudSat reflectivity-height distributions for 17°S-27°S and 70°W-80°W a) MAX N_d , b) MIN N_d ; and 20°S-30°S and 80°W-90°W c) MAX N_d , d) MIN N_d . The colors indicate the percentage of the total pixels at each altitude; their summation over reflectivity equals total cloud fraction at that altitude. The dashed line indicates mean MODIS-derived cloud top height. Note different y-axis ranges for top and bottom panels.

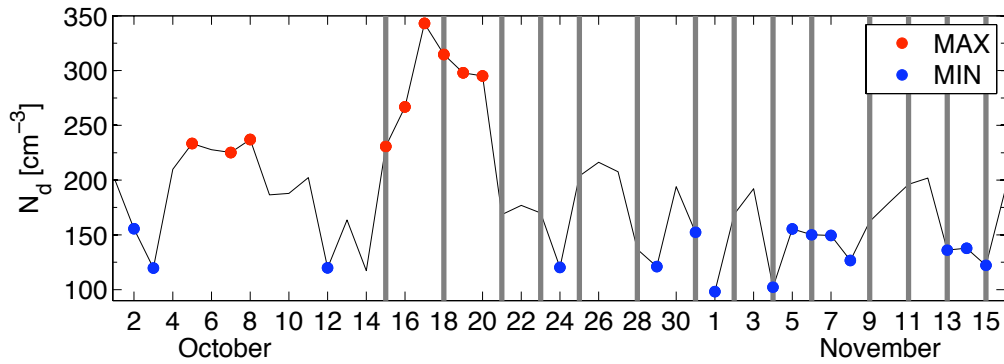


Figure 12: VOCALS-REx spatial-mean N_d time series over the Arica Bight with MAX and MIN cases highlighted in red and blue respectively. NCAR flight days are indicated with grey bars. Twin Otter flights to Point Alpha (75W, 20S) coincided with MAX/MIN cases on Oct. 16, 18, 19, 24 and Oct. 29.

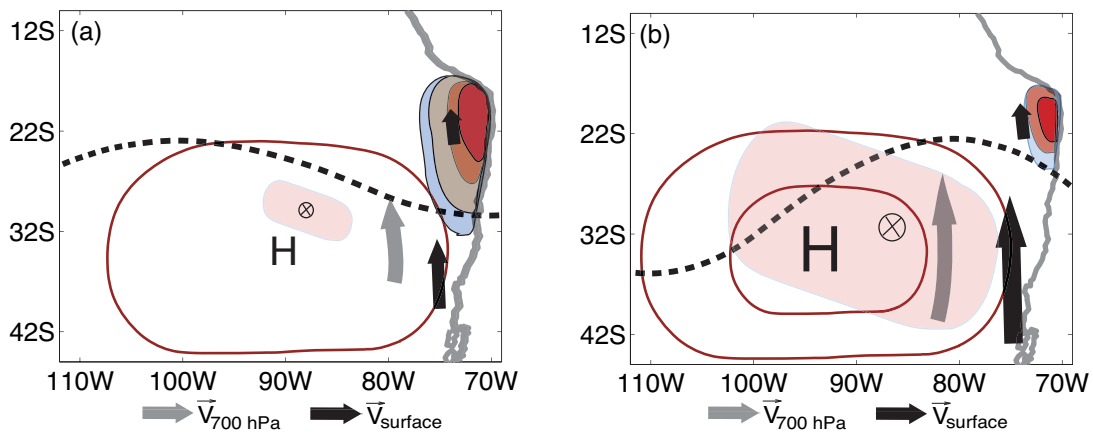


Figure 13. Schematic of a) MAX N_d , and b) MIN N_d large-scale meteorology. The 500hPa geopotential height is indicated by the dashed line, the sea-level pressure by red contours, subsidence by the shaded area, 850 hPa and surface winds by grey and black arrows respectively. The color shading over Arica Bight indicates the region with large N_d .

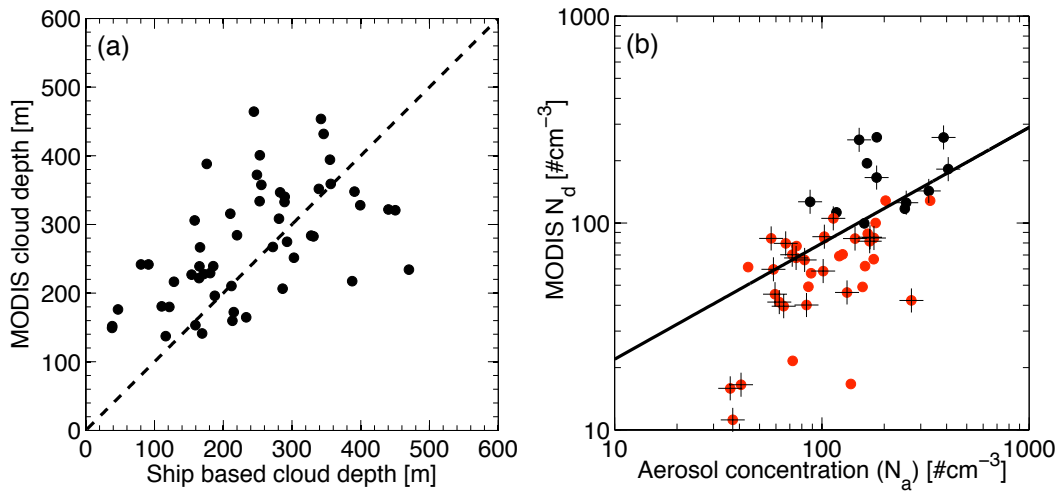


Figure 14. (a) MODIS-derived cloud depth (25 km^2 average) versus ship-based cloud depth (hourly averaged; ceilometer cloud fraction >0.9), and (b) MODIS-derived N_d (25 km^2) versus ship-based accumulation-mode ($r > 0.1 \mu\text{m}$) aerosol concentrations (hourly-averaged; no restriction on ceilometer cloud fraction). Black dots indicate samples east of 80°W and crosses are samples for which the bias-corrected MODIS H_{sat} is within 70 m of H_{ship} . The black solid line represents the best-fit line for all values with $N_d > 50 \text{ cm}^{-3}$. Sampling domain covers $0^\circ\text{-}30^\circ\text{S}$, $72^\circ\text{W-}90^\circ\text{W}$. Fig 1a and 1b were constructed with 51 and 48 samples respectively.